CFD Simulation of High-Speed Trains: Train-induced Wind Conditions on Trackside Installations

Vahid Sarafrazi[1], Mohammad Reza Talaee[1*]

[1]School of Railway Engineering, Iran University of Science and Technology, Tehran, Iran

ARTICLE INFO	A B S T R A C T
	High speed trains in operation encounter aerodynamic effects of the air flow as well as slipstream effects. A high-speed train passing under a structure or object makes sudden impacts on aerodynamic forces acting on that object. Therefore, this issue needs to be considered in the design of structures and installations to be built around high-speed rails. In this study, a numerical simulation with moving mesh and k-epsilon turbulence model is carried out in FLUENT engineering software in order to investigate the aerodynamic and the slipstream effects for a high-speed train in motion on overhead and trackside installations with the objective of preventing aerodynamics-induced damage. This simulation is conducted in two scenarios of absence and presence of aerodynamic brake on topside of the train. In the end, ABAQUS finite element software is used to determine the maximum stress exerted on objects (installations) positioned at different distances from the rail, and the results are compared with the maximum allowable stresses to determine a minimum permissible distance between installations and high-speed trains.

1. Introduction

The past few years have been witness to continuous global development of high-speed railway systems regarding the speed of trains as well as the track number. Within a number of developed countries including Italy, Japan, Sweden, and Germany, the mean speed of high-speed trains is currently over 150 (km/h). The best records of train speeds belong to Japan's high-speed railway system, and the highest record, 604 (km/h), has been achieved in 2015 by a seven-car maglev train on a test track in Yamanashi Prefecture [1]. It should be noted that the actual maximum speed of high-speed trains operating in Japan is 430 (km/h). Iran's first high-speed rail linking Tehran, Qom, and Isfahan is currently under construction. This track is 412 (km) long and its train schedule is designed based on the speed of 300 (km/h).

Aerodynamic forces formed by the passage of a train are in proportion to the speed of the train (square of this number). Therefore, at such high speeds, these forces need to be duly considered to avoid potential risks and problems. The failure to address these potential problems before operation of high-speed railway can impose great safety risks on the project. The aerodynamic pressure is the effect of a passing object that creates severe flow and pressure fluctuation in its environment. The transient air velocity that is made by a moving train is scientifically termed as slipstream velocity. The effects of slipstream for a moving train on trackside and overhead objects, structures, and installations are of great importance. According to the standards of European Union (TSI, 2008/232/CE) [2], slipstream velocity created in the trackside due to passage of a train (with all the wagons attached) in an outdoor environment at the speed of 190 to 249 (km/h) or 250 to 300

*Corresponding author
Email address: mrtalaee@iust.ac.ir

(km/h) would not exceed, respectively, 20 (m/s) and 22 (m/s). These slipstream velocity thresholds are specified for the points 0.2m above the rail, and 3m away from the rail centerline. Also, the peak-to-peak pressure load measured at heights 1.5m to 3m above the rail and 2.5m away from the rail centerline during the passage of a full length train (including the head, couplings and tail) in the open air at the speed of 190 to 249 (km/h) and 250 to 300 (km/h) could not exceed, respectively, 720 (Pa) and 795 (Pa). Scholars have investigated the subject of slipstream for trains since 1970. So far, a number of different methods have been developed for studying this subject [2]. Early aerodynamic pressure results obtained by Hara et al. [3] using hot-wire anemometers show significant variations in slipstream velocity near the nose of the train as well as the train tail [3]. Numerical work on slipstream is performed in Hemida et al. (2010) [4] that the experimental setup of a rotating rig is investigated and in Hemida et al. (2014) [5], the straight case is simulated, both simulated with Large-Eddy Simulation. The simulations in [5] are performed on a 5-car ICE2 train model at 1:20 scale and the results are given with different platform heights. The results are, for example, given for the time averaged velocity at a two meter distance of the track center (full-scale) and show high slipstream velocities as the train is passing the platform. This location is close to the train surface and therefore, the highest amounts of slipstream velocity occur within the boundary layer domain. Muld [6] considered a version with 1:50 scale for train geometry, in which a train had two cars, while the other had only one car and a half. According to the free stream velocity as well as the characteristic length scale of the trains' geometry (three meters for full-scale, while 0.06 meter for 1:50 scale), the Reynolds number was calculated to be 60,000 for both of the train geometries. The author took advantage of Proper Orthogonal Decomposition as well as Dynamic mode Decomposition for decomposition of simulated flow field. There were a number of resemblance and divergence after flow separation at the back of train. The vortex shedding was the mere flow structure that existed in both geometries. Measuring the slipstream effects of the two trains was also conducted. Due to the fact that a train was wider than another, a closer measurement position to the surface of the train was selected, and accordingly, the slipstream velocity incremented

near the peak value, while there was not much variation away from the peak value. In this research, the influences of the length of train over the flow structure were also studied. It was revealed that a variety of wave lengths as well as frequencies exist for flow structures. Nonetheless, flow topology and dominant flow structures were the same. Baker et al. [7] also carried out some empirical research to measure the transient loads imposed by passing trains on the trackside structures. They compared the empirical outputs and the present standards. It was revealed that England's standards were over-conservative. They attributed this issue to the fact that basis of these standards are tests and calculation carried out for the railways and trains of continental Europe, which are somewhat larger than standard dimensions of England's railway system. They provided two methods for modification based on train dimensions and both methods predicted the experimental results better than the standards. Finally, they provided some formulations and experimental results regarding the aerodynamic loads acting on different structures to facilitate the future efforts aimed at revising the standards. In the study of Dhanabalan [8], Detached Eddy Simulation techniques were used in order for simulation of flow in a 1:15 scaled model of a train (ETR500 high speed train). A variety of configurations were tested in the simulation (the same configurations as those used on track and within the wind tunnel). Afterward, the simulation outputs were compared to the outputs of experimental tests that were conducted for Torino-Novara line (a high-speed line). Yang et al. [9] organized a number of experimental tests and numerical simulations in order to study the effects of a train passing under a bridge on the resulting aerodynamic loads acting on the structures overhead. Numerical simulations were done with moving mesh and two-equation turbulence models in FLUENT software. They studied the pressure distribution and the correlation of pressure and the speed of train, and showed that a train passing under a bridge creates a transient and complex turbulent flow between the train and the bridge, which needs to be duly considered in the design process of overhead structures.

An overview of the previously-conducted research results shows that aerodynamic forces induced by high-speed trains should not be neglected and that standards concerning this

issue only express a permissible range for the wind speed created at the trackside. In this study, the FLUENT software is used to simulate a high-speed train with normal geometry and also with aerodynamic brake. These two models are then used to study the aerodynamic and slipstream effects of train passage on overhead and trackside structure and installations such as pipelines, electric cables, etc. In contrast with other studies, train is modeled in motion and in two scenarios of absence and presence of aerodynamic brake. The outcome of this work is the minimum permissible distance of objects to be installed at trackside and overhead of a high-speed rail.

2. Geometric Modeling

It is needed to conform to the following instructions. The first step of an accurate simulation is to determine the accurate geometry of the object to be simulated. In this study, the geometry of main surfaces of the train is extracted from the ICE train model provided by Bombardier factory. This model comprises of a leading motor car and a trailing control car. The train is considered to be in motion. The center of train and the rail-top were pinpointed as the coordinate system origin. The modeled train had a length of 35.55m, a width of 3m, a height of 3.75m, and a cross-sectional area of 8.185 square meters. The train's characteristic length equals to its hydraulic diameter (d_h). In this model, the hydraulic diameter is considered to be 3m [8]. To reduce computation load, car placement is assumed to be in form of Figure 1.

Figure 1. Car placement in the 2-car high-speed train [8]

Figure 2 displays the model geometry in SOLIDWORKS software and Figure 3 reflects cross-sectional dimensions of the model. After defining the domain in SOLIDWORKS software, model is imported into ANSYS software. The PRB points of Figure 3 are the places at which speed variations over time are measured. In this study, the high-speed train is modeled in two modes, the normal geometry and with aerodynamic brake.
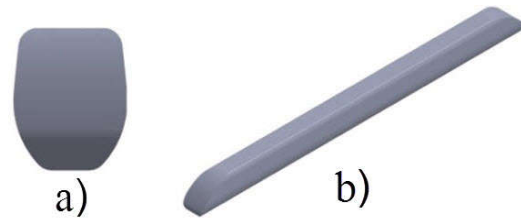

Figure 2. Model geometry in SOLIDWORKS software: a) cross-sectional view b) 3D view
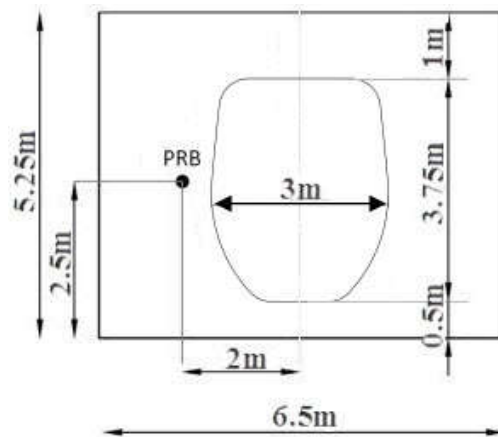

Figure 3. Cross-sectional dimensions of the model developed in SOLIDWORKS software

Extensive simulation research has been conducted to investigate the effect of aerodynamic brake and design the brake panel position [10-13]. In light of the research carried out by Puharic et al. [14], where the distribution of the aerodynamic force driven by the brake panels was studied, it became clear that the brake panel positioned at the beginning creates the greatest aerodynamic drag, whereas the brake panels located in the subsequent positions create a smaller aerodynamic force and contribute less to the generation of brake force to stop the train. Hence, a brake panel with the dimensions specified by Puharic et al. is modeled and examined at the position. Figure 4 shows a view of rectangular brake panel modeled with a length of 1.5m, a thickness of 0.15m, and a height of 0.9m on top of the train with a six-meter distance from the nose.

2.1. Computational domain of the study

Computational domain should be extensive enough in order to prevent inaccurate boundaries from leaving substantial effects on simulation.
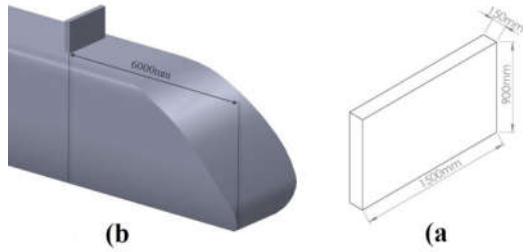
Figure 4. A view of the train with aerodynamic brake: a) dimensions of brake panel b) distance from the nose

Investigating a passenger wagon, Axelsson et al. [10] showed that inappropriate distance may create an improper pressure field around a train. Manhart and Wengle [15] presented the computational domain for the flow around a cuboid. Krajnovic [16] introduced a more extensive computational domain around a train. The computational domain's numerical values in this study were selected according to those proposed by [17] so as to avoid the development of an inappropriate pressure field.
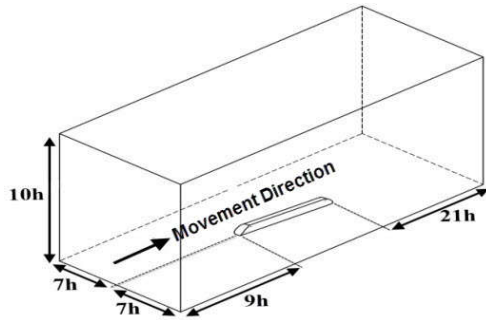

Figure 5. A Computational domain considered for the geometric model of high-speed train

The domain considered in this study consists of a model train placed on a flat surface Figure 5 and the computational domain around the train consists of a cuboid with a height of 10h (h= train height). The train's front side and back side regions also need to be long enough to prevent inlet and outlet walls from making substantial effects on analysis. Therefore, these regions are considered to be 9h and 21h in length.

2.2. The used turbulence model

Presence of speed and pressure fluctuations in Navier-Stokes equations of turbulent flows makes them more complex than those of laminar flows. It is possible to determine velocity (along direction x) through adding the time-averaged component to fluctuating component. Similarly,

pressure can be measured by adding the time-averaged component to fluctuating component. Ignoring the gravity, Navier-Stokes equation of an incompressible flow along direction x can be simplified as Equation (1): [17]

$$\rho\left\{\frac{\partial u}{\partial t} + \bar{u}\frac{\partial u}{\partial x} + \bar{v}\frac{\partial u}{\partial y} + \bar{w}\frac{\partial u}{\partial z}\right\} = -\frac{\partial p}{\partial x} + \mu\left\{\frac{\partial^2 u}{\partial x^2} + \frac{\partial^2 u}{\partial y^2} + \frac{\partial^2 u}{\partial z^2}\right\} \tag{1}$$

Replacing the velocity and pressure parameters with the sum of time-averaged and fluctuating components gives the Navier-Stokes equation for turbulent flow along direction (x) as Equation (2):

$$\rho\left\{\frac{\partial \bar{u}}{\partial x} + \bar{v}\frac{\partial \bar{u}}{\partial y} + \bar{w}\frac{\partial \bar{u}}{\partial z}\right\} = -\frac{\partial \bar{p}}{\partial y} + \mu\left\{\frac{\partial^2 \bar{u}}{\partial x^2} + \frac{\partial^2 \bar{u}}{\partial y^2} + \frac{\partial^2 \bar{u}}{\partial z^2}\right\} - \rho\left\{\frac{\partial}{\partial x}\bar{u}'^2 + \frac{\partial}{\partial y}\bar{u}'\bar{v}' + \frac{\partial}{\partial y}\bar{u}'\bar{w}'\right\} \tag{2}$$

Simulation of turbulent flows with eddy currents is associated with a number of problems. These currents are of different length scales as small as 1μm. Incorporation of all these currents requires a mesh so small that would be practically unsuitable for processing with today's computers. To deal with this issue, engineers have to use the average values of flow characteristics with the help of time-averaged forms of Navier-Stokes equation. Doing so creates 6 unknowns $\rho\bar{u}'^2, \rho\bar{v}'^2, \rho\bar{w}'^2, \rho\bar{u}'\bar{v}', \rho\bar{u}'\bar{w}', \rho\bar{v}'\bar{w}'$ called Reynolds stresses, which express the flow characteristics but are impossible to be directly determined. One of the turbulent models is the zero-equation model that cannot predict the effects of the turbulences created at upstream flow on downstream flow. From mathematics viewpoint, the system of flow equations obtained from modeling of the turbulent flow of type zero is an equation almost identical to that pertaining to laminar flows. Another turbulence model is the Spalart model, which is a new, one-equation model. No claim has been made so far with regard to the suitability of this model for all complicated engineering flows. Owing to its inability to adapt itself with the rapid changes in length scales, this model has always been criticized. These intense changes may be observed especially in the abrupt changes from wall-bounded flows to free-shear flows (similar to the discharge of a jet with limited dimensions

into an environment with infinite dimensions such as the atmosphere). On the other hand, the Spalart model suffers from serious defects in terms of the ability to allow for the effects of sub-models (e.g. in combustion problems or those involving free motion). Another group of turbulence models is two-equation models that have received a great deal of attention particularly in recent years as the foundation of many studies addressing turbulent flow modeling. This model yields proper responses for a wide spectrum of problems. However, for problems that involve intense non-isotropies and non-equilibrium effects, this model will achieve responses that are to some extent over diffusive. The popularity of this method in the simulation of heat transfer and industrial flows stems from its power in solving problems, reasonable cost, and its notable accuracy for most of the problems in the field of turbulent flow. On the other hand, selecting an appropriate turbulence model hinges on considering such factors as flow physics, a definite technique for a certain group of problems, the necessary accuracy, the existing computational resources, and the time needed for simulation [18]. Ogawa and Fujii [19], Howe [20] investigated the effect of the pressure wave resulting from train movement inside the tunnel. Yang et al. [9] studied the response of air pressure velocity caused by train movement on the bridge structure over the train. Biadgo et al. [21] simulated the effect of lateral wind on high-speed train stability. Fluent model as well as the two-equation flow turbulence model $(k - \varepsilon)$ were utilized in all the research mentioned above. Whereas this research centers on the forces exerted on obstacles and in light of the advantages and disadvantages mentioned for two-equation models, the standard $(k - \varepsilon)$ method is employed in this study.

2.3. Boundary conditions

Figure 6 shows the inlet, outlet, and symmetry boundary conditions used for the train model. The walls are modeled with a no-slip boundary condition. Meaning that tangential velocity is zero. Walls are solid and impermeable, which means that normal component is zero, as no liquid can pass through the walls. In this modeling, there are two types of walls: fixed and moving. For moving walls, the near-wall liquid particles move with the same speed as the wall does. All components pertaining to the train itself are assumed to be

moving, and all other walls, the ground, the surrounding air and all objects are assumed to be fixed [7]. The turbulence of near-wall particles are expressed with non-equilibrium wall functions [21]. Assuming a moving train means that a proportional motion exists between the train and the ground. Velocity and scalar parameters at inlet boundary are determined using the velocity inlet boundary condition. In computational fluid dynamics, discretization of equations should be followed with application of an initial condition, so in this case, air flow velocity at inlet boundary is initialized with zero, and solution of flow equation begins from this boundary.
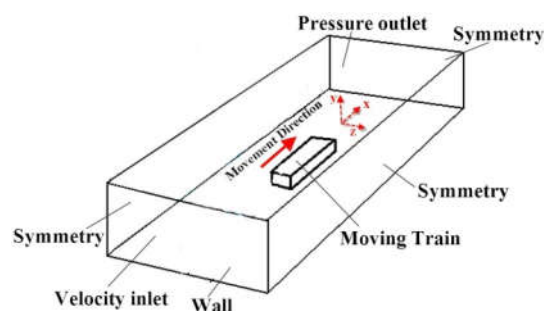

Figure 6. The boundary conditions considered for the moving train

For the train itself, flow is of external type and external flows have a low level of turbulence. Velocity component of train in-motion was presumed to have a form of turbulence factors considered for the train (i.e. turbulence intensity and turbulence length scale). These factors are constant in time by assumption. In a study by Casey et al. [22], turbulence intensity as well as turbulence length scale were considered 3% and $(0.1d_h)$, respectively. The outlet boundary condition is of the pressure outlet type. Therefore, the static pressure at the outlet boundary needs to be determined. The side and upper surfaces of the air around the train are modeled with symmetry boundary conditions. In the symmetry boundary conditions, the vertical component of velocity and normal gradients for the whole variables at the boundary are considered to be zero. Consequently, defining symmetry boundary conditions for a surface means that at that surface all fluxes are zero. Moreover, since the shear stress at symmetry surface is zero, it can be argued that in turbulent flow symmetry boundary condition satisfies the sliding wall boundary condition [8].

2.4. Meshing

Achieving a high quality mesh with right number of elements requires a good knowledge about different parts of computational domain to assign some uncritical parts with a mesh as coarse as possible. Those surfaces that are prone to sudden geometric changes, such as nose and tail of the train, probably need a mesh refinement procedure. As mentioned in the first section, this study considers the train to be moving. Thus this train needs to be meshed with moving elements. Moving meshes can be divided into two categories: sliding mesh, and dynamic mesh. The use of sliding mesh allows to partition the problem into discrete sections moving relative to each other. These motions can be rotational or transitional. Assuming relative motion between fixed and moving parts (like stators and rotors) leads to use of transient analysis for simulation of a period of motion, but dynamic meshing allows the boundaries of an area to be moved within the same region. In this way, boundaries may have rotational, transitional, or deformational movement with respect to each other. Many problems can be solved with either of these methods. Dynamic meshing can also be used for cases where mesh will undergo a deformation or when mesh movement is a function of the solution. The movement of piston inside cylinder engine is an example of the cases where dynamic mesh provides better analysis. In FLUENT, this type of meshing can be used for flow models where domain boundaries are mobile and thus domain transforms with this motion. Dynamic meshing can be used for single-phase or multi-phase flows. It can also be used for steady states where mesh motion can contribute to reach to a better solution. In the FLUENT software, mesh will be updated automatically at every time step, according to the boundary position. To use dynamic mesh, a starting volume mesh needs to be provided and motion of each moving region of the model needs to be described. FLUENT allows these motions to be defined with boundary profiles or with the help of user-defined functions (UDFs). In cases where model includes both moving and stationary regions, these regions need to be identified by grouping them into their respective cell zones in the initial volume mesh. In addition, the regions that will be deformed as a result of motion need to be grouped into separate zones in the starting volume mesh. The use of trimmed hexahedral grids with prism layers in near wall

surfaces has yielded good wall behavior results [23]. To achieve a better structure, external hexahedral grid in the area surrounding the train is subjected to a mesh refinement process. It appears that the train's nose and its front side region and train's tail and its backside regions also need a mesh refinement procedure. Considering the importance of slipstream effects on trackside and overhead objects, the mesh of these objects should also be refined. The mesh refinement used in this study is the preferential discretization method proposed by Manhart and Wengle (1993) [15]. The refinement domain consists of a cuboid with $8.97d_h$ of length, $4d_h$ of width, and $1.83d_h$ of height surrounding the train and another cuboid with a length of $0.65d_h$, a width of $4d_h$ and a height of $0.42d_h$ at nose and tail of the train.
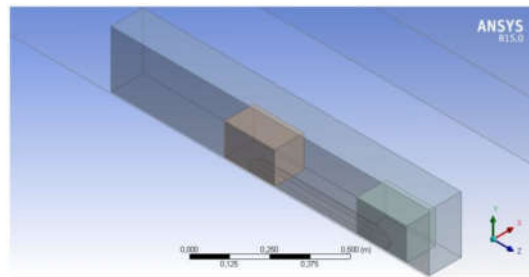

Figure 7. Mesh structures used for the simulation

Figure 7 shows a view of the mesh refinement zones used in the course of simulation. In this simulation, medium mesh has a base size of 0.5m; the relative least possible size is twenty percent of the base size, while the relative target size is considered to be as much as eighty percent of the base size. The regions deemed less important are given a coarser mesh to avoid unnecessary computation and decrease the time of analysis. In this simulation, prism layer thickness is 25%, prism layer count is 5, prism layer stretching is 1.2, and a slow growth rate is assumed to create layers with equal mesh size [6]. Figure 8 shows a view of the mesh in regions near the train, and Figure 9 shows the spatial distribution of elements.
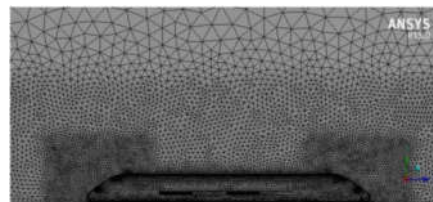

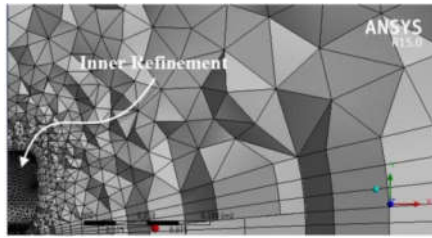Figure 8. Trimmed hexahedral mesh used for the regions surrounding the high-speed train

Figure 9. Spatial distribution of elements from a cross-sectional view

To examine the grid independence of the solution, three different cases were considered namely the coarse grid that was composed of 1.3 million elements; the medium grid composed of 2.8 million elements; and finally, the fine grid made up of 3.4 million elements. Figure 13 shows the dimensionless variations of air velocity by time.

3. Simulation and Result

According to definitions of the International Union of Railways (UIC), high-speed trains are those that provide speeds of higher than $200\ km/h$. In this simulation, train speed was considered to be $56 m/s$. Density of Air is $1.225\ kg/m^3$, viscosity is $18.27\ \mu Pa.s$, and hydraulic diameter is 3m. Therefore the Reynolds number was calculated to be 11264000. Passage of high-speed train under the object was simulated in two scenarios of absence and presence of aerodynamic brake. The modeled objects were two cylinders with diameter of 2in or 5.08cm and length of 5.25m. One object was positioned horizontally at a point 5.25m above the ground, and the second one was positioned vertically next to the first object. The time step was 0.0006 seconds and the entire analysis took about 10 days of processing. This processing was carried out by a 16-core computer with 16 GB of memory. Table 1 shows the configurations of FLUENT solver in this simulation.

As Figure 10 shows, the maximum velocity is on the train's body, and velocity reduces radially with a distance from the nose. Once train passes an object, its slipstream turbulence can be seen as vortices that fade away as the tail becomes farther. According to Figure 11, the presence of aerodynamic brake has led to emergence of maximum velocity at the back of the brake panel and creation of a vortex flow around the aerodynamic brake. To determine the accuracy of the results, the variations of the dimensionless values of air velocity (in relation to train velocity) in terms of distance were compared to those in the study conducted by Yang et al [9], Figure 12.

Table 1. Configurations of FLUENT software

Category	Used Configurations
Solver	Pressure-based
inlet and outlet boundary conditions	Pressure outlet has a zero static pressure (stationary subdomain)
	Velocity inlet has a zero velocity and pressure outlet has a zero static pressure (moving subdomain) too.
	No-slip; y+ at the train sidewalls gets to its maximum amount, and train surfaces value of 175, wall functions will be implemented if the grid becomes too coarse to resolve the laminar sub layer (Ground surface, tunnel Wall)
Solving method	Pressure-velocity (SIMPLE)
Discretization method	Least Squares Cell Based
	Second order Implicit, Non-Iterative Time Advancement (NITA)
	Cell zone stipulations Moving mesh for train subdomain

This comparison makes it perfectly clear that the results are acceptably similar in terms of behavior. Further, to re-investigate the accuracy of results, the dimensionless variations of air velocity extracted by the experiments of Gilbert et al. [24] were compared to the simulation results of this study as per Figure 13, where train velocity is equal to $140\ km/h$ and the train nose as well as the train tail reached the measurement point (PRB) respectively at 4 seconds and 7.5 seconds.
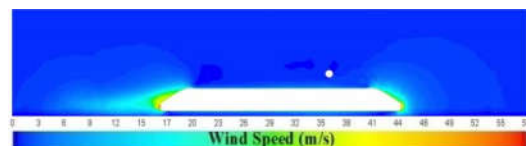

Figure 10. The velocity profile at cross-section of the train once its nose passes the overhead object without aerodynamic brake
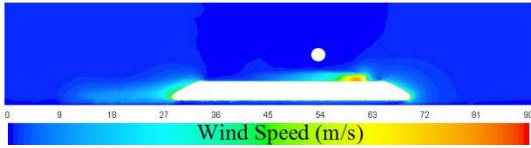
Figure 11. The velocity profile at cross-section of the train once its nose passes the overhead object with aerodynamic brake
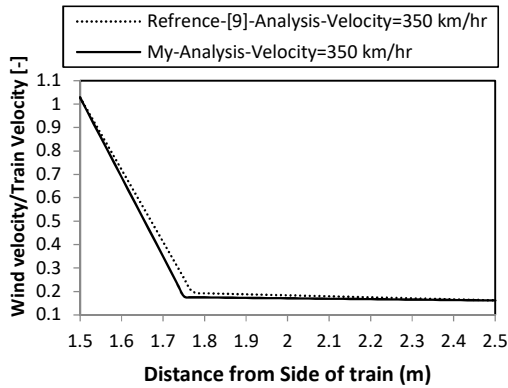

Figure 12. Comparison of trackside normalized slipstream velocity profile obtained in this study with the one obtained in [9]
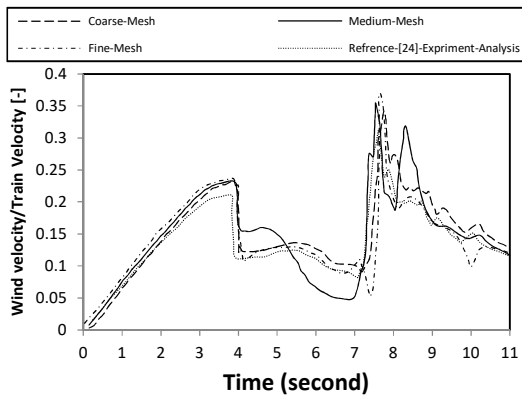

Figure 13. Comparison of the dimensionless velocity at the measurement point obtained through experimentation by Gilbert [24] and that in this study for different grids

The pinnacle of the pressure wave obtained by simulation does not match with that obtained from experimentation. This is caused by the simplified assumptions in the discretization and mathematical modeling of flow equations, including Equation (1) and Equation (2). Moreover, wind velocity before the train nose passes from the measurement point (time period less than 4 seconds) and after the train tail passes from the measurement point (time period more than 7.5 seconds) was greater than that measured experimentally by Gilbert et al. Of course, the pinnacle of the pressure wave involves uncertainty in the research results of Gilbert et

al., which were obtained by experimenting 25 trains. As Figure 14 shows, in this analysis, central axis of the train coincides with the centerline, so external body of the train is 3.75m vertically and 1.5m horizontally away from the center of the coordinate system.
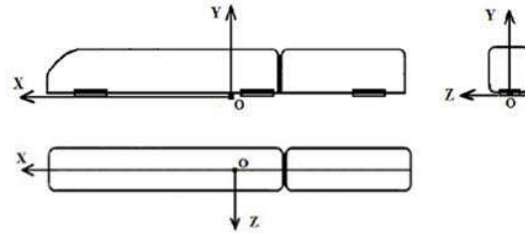

Figure14. Position of the coordinate system with respect to train model

As a result, in Figure 15, the horizontal axis does not start from zero and its starting value is 3.75m, and according to the coordinate system shown in Figure 14, this value represents the train's roof. According to Figure 15, as time passes, velocity of slipstream created on top of the train increases. On the other hand, this parameter decreases with the distance from the train's body. Figure 16 shows the variations of velocity profile with time at the measurement points shown in Figure 3. According to this figure, the critical points are the moments when nose and tail pass under the object. Next, the effect of different train speeds over velocity of slipstreams created on the trackside is investigated. For this purpose, train speed was increased to 250, 300 and 350 km/h, and the results pertaining to slipstream velocity at the trackside were studied. It should be noted that this part of study was also carried for both scenarios of absence and presence of aerodynamic brake.
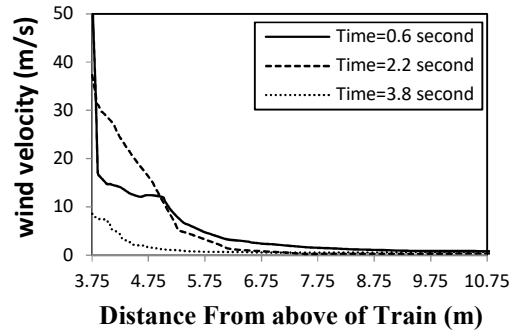

Figure 15. Variations of velocity in terms of distance from the train's body when its nose, mid-section or tail is passing the object
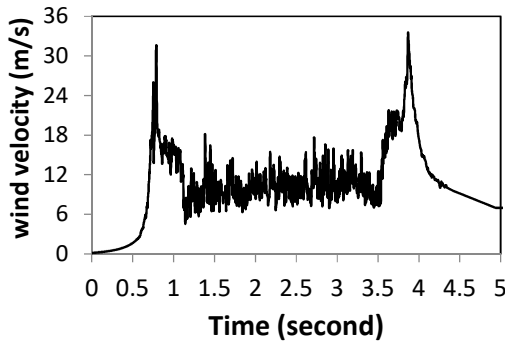
Figure 16. Variations of velocity profile with time at the measurement point (PRB)

As Figure 17 shows, the measurements were carried out along two lines: an overhead line starting from (12.5, 3.75, 0) and ending at (12.5, 12.5, 0), and a trackside line starting from (12.5, 0, 1.5) and ending at (12.5, 0, 21.5).
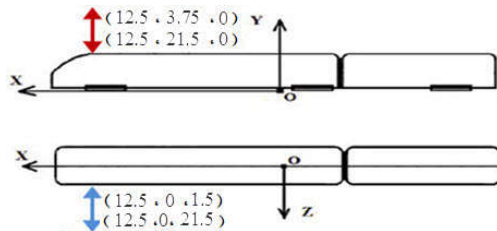

Figure 17. Coordinates and position of measurement points at trackside and overhead

These measurements gave the variations of different parameters in terms of distance from the train. Next, the changes in the velocity of slipstream acting on overhead object during the passage of nose were examined for four different train speeds. The changes in velocity of slipstream acting on overhead object are depicted in Figure 18.
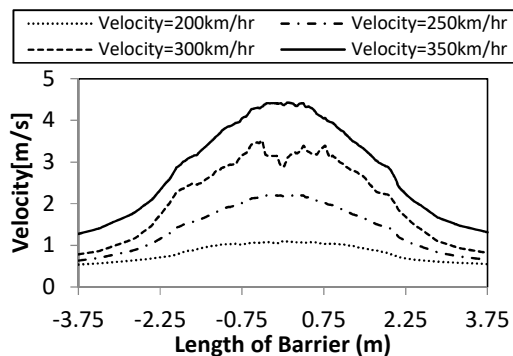

Figure 18. Changes in velocity of slipstream acting on overhead object during the passage of train's nose

As this figure shows, as train speed increases, so does the velocity of slipstream created above the train. Figure 19 shows the changes in pressure coefficient at the location of object due to passage of train with four different speeds. As can be seen, the slipstream velocity and pressure due to train passage increases after the train speed escalates.
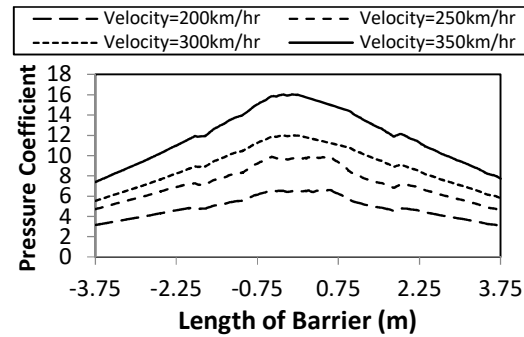

Figure 19. Coordinates and position of measurement points at trackside and overhead

As a result, this phenomenon could impose some dangers in case the train is moving with a higher speed. Figure 18 and Figure 19 show the changes in velocity profile and pressure coefficient at the location of object located above the passing train. These results pertain to the moment when the train's nose passes the point of measurement. As Figure 18 and Figure 19 show, velocity and pressure coefficient values are highest at the middle of the object and decrease with the distance from the center. The pressure exerted by the wind speed of (V_w) can be expressed with Equation (3):

$$P = \frac{1}{2}\rho C_p V_w^2 \tag{3}$$

Where (ρ) denotes air density, (C_p) is aerodynamic pressure coefficient, and (P) denotes the pressure due to movement of air during train passage. Having the air velocity variations in terms of distance from the train's body, the wind speed induced stress can be calculated in terms of vertical and horizontal distance from the train's body. Figure 20 and Figure 21 show the distribution of applied stress in terms of distance from the train's body in the region above the train and in the trackside, respectively. Again, these results pertain to the moment when the train's nose passes the point of measurement.
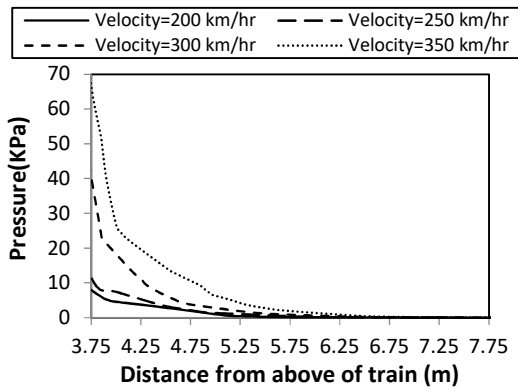
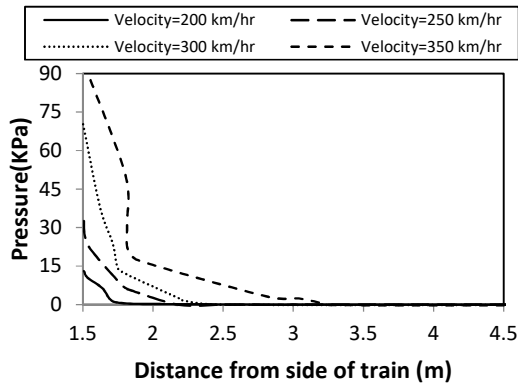Figure 20. Variations of pressure in terms of distance from the train's body in the region above the train

Figure 21. Variations of pressure in terms of distance from the centerline in the trackside

over its cross section will be as shown in Figure 26.
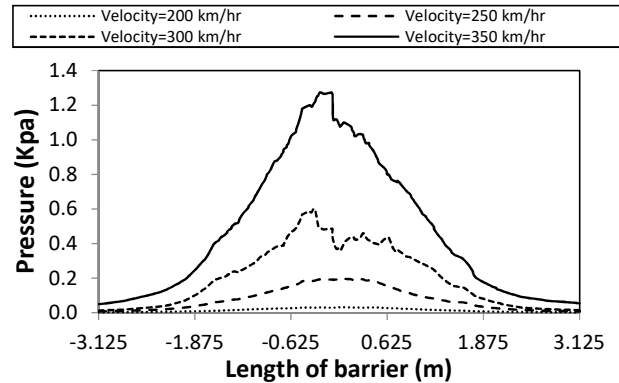

Figure 22. Distribution of pressure acting on the object positioned above the train for different train speeds
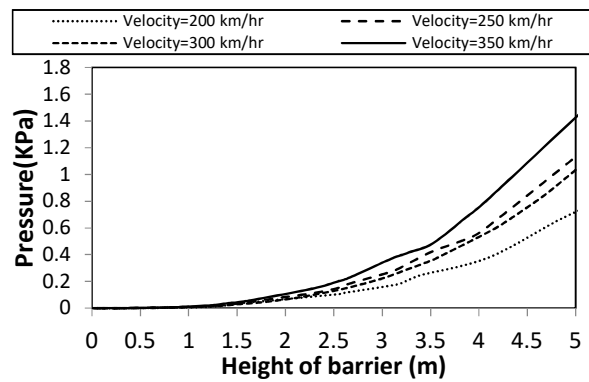

Figure 23. Distribution of pressure acting on the object positioned on the trackside for different train speeds

Figure 22 and Figure 23 show the distribution of pressure acting on the object positioned above the train and on the trackside, respectively. Like before, these results pertain to the moment when the train's nose passes the point of measurement. To verify the accuracy of maximum pressure acting on overhead object, in Table 2, these values are compared with the values provided by [2] in regard with maximum pressure due to wind speed.

Figure 24 and Figure 25 show the diagram of the pressure induced in the objects positioned overhead and in the trackside by the passage of the train with an aerodynamic brake. It should again be noted that these results pertain to the moment when the train's nose passes the point of measurement. As Figure 24 and Figure 25 show, presence of aerodynamic brake has reduced the peak pressure acting on nearby objects [25]. For a cylindrical gas pipeline, distribution of load

Table 2. Maximum pressure due to wind speed induced by train passage [2]

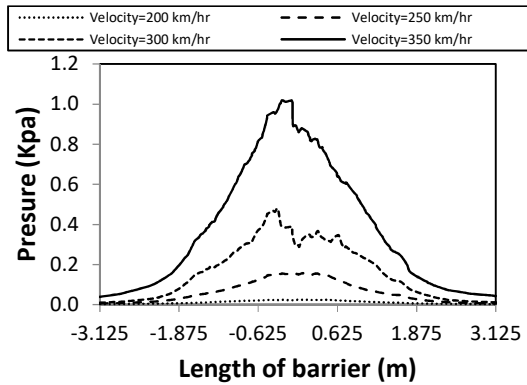| Train speed	Maximum pressure variation
Maximum speed of between 190 and 250 (km/h)	720Mpa
Maximum speed of 250 (km/h) and higher	795Mpa

Figure 24. Distribution of pressure acting on the overhead object during the passage of the train equipped with aerodynamic brake at different speeds
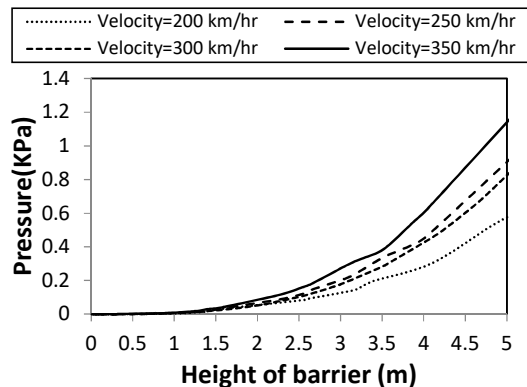

Figure 25. Distribution of pressure acting on the trackside object during the passage of the train equipped with aerodynamic brake at different speed
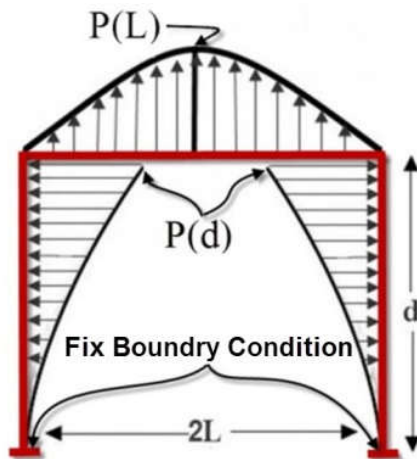

Figure 26. Distribution of slipstream-induced load on the overhead and trackside objects

4. Determination of Permissible Distance

To find the minimum permissible distance of objects from the train, load distribution obtained in Figure 26 is used for finite element modeling with ABAQUS software to calculate the amount of stress exerted on the objects. This stress was then compared with the maximum permissible stress for a cylindrical pipe with a diameter of 2 inches (5.08 centimeters). The pipe was assumed to be made of steel ST35 with minimum yield strength of 220Mpa (According to DIN2448; regulations for pipes with diameters of more than 40 millimeters) [26]. The simulations results were used to determine the distances d and L in Figure 26 such that the pipe would be immune to aerodynamics-induced damage. To apply the static load on the objects, the pressure distributions obtained from the FLUENT software Figures 23-26 were curve fitted for the maximum speed of 350 km/h. The results are Equation (4) and Equation (5) for trackside and overhead objects in the absence of aerodynamic brake, and Equation (6) and Equation (7) for trackside and overhead objects in the presence of aerodynamic brake on the train. The finite element software was used to apply these pressure distributions on the objects Figure 27.

$$p = 9y^3 + 13.1y^2 - 11.3y \tag{4}$$

$$p = 9x^6 - 2.8x^5 + 77.9x^4 + 38.6x^3 - 490.4x^2 - 116.9x + 1.128 \tag{5}$$

$$p = 8.1y^3 + 11.9y^2 - 10.2y \tag{6}$$

$$p = -3.6x^6 - 2.5x^5 + 70.8x^4 + 35.1x^3 - 445.8x^2 - 106.2x + 1.025 \tag{7}$$
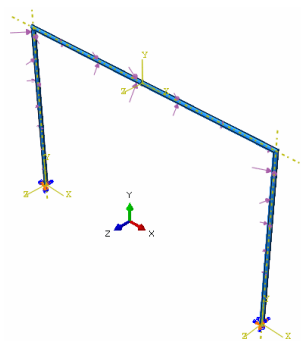

Figure 27. Distribution of slipstream-induced load on the overhead and trackside objects in ABAQUS software

After conducting an analysis with finite element software and extracting the stresses, the maximum values of stress in two 6.25m long objects, one positioned 6.25m above the ground and the other one positioned 4.25m farther the

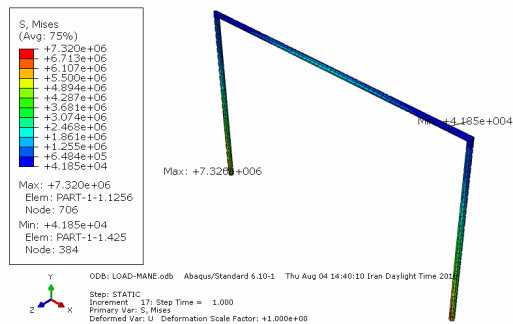centerline were obtained as depicted in Figure 28 and Table 3.

Figure 28. Distribution of slipstream-induced stress in the overhead and trackside objects in the absence of aerodynamic brake (mode 1)

Table 3. Maximum stress formed in overhead and trackside objects (mode 1)

Maximum stress	Pascal
In the absence of aerodynamic brake	7.32×10^6
In the presence of aerodynamic brake	6.65×10^6

According to these results, the maximum stress has occurred at the bases. Subsequently structural failure can be expected to start from those positions. Due to the insignificant magnitude of this parameter, in this mode, the distance of 6.25m from the ground and 4.25m from the centerline can be assumed as a good distance for the placement of installations (pipes, etc.) around the high-speed rails. To find the minimum permissible distance, pressure profiles of two 6.25m long objects, one positioned 4.85m above the ground and the other one positioned 3.32m away from the centerline were extracted. Again, the finite element software was used to apply the extracted pressures on the objects. Figure 29 and the results of Table 4 were obtained.

Table 4. Maximum stress formed in overhead and trackside objects (mode 2)

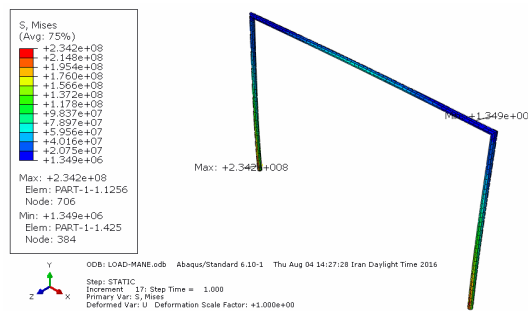| Maximum stress	Pascal
In the absence of aerodynamic brake	2.34×10^8
In the presence of aerodynamic brake	2.12×10^8

Figure 29. Distribution of slipstream-induced stress in the overhead and trackside objects in the absence of aerodynamic brake (mode 2)

5. Conclusions

This study examined the effect of slipstream caused by passage of high-speed trains on the overhead and trackside installations such as pipelines or power cables. This effect was studied in two scenarios of absence and presence of aerodynamic brake on topside of the train. Examination was carried out through a number of simulations conducted using computational fluid dynamics and FLUENT software. The validity of computational model was assessed through comparing the modeling results and the experimental results .This comparison made it clear-cut that the results are acceptably similar in terms of behavior. The overall outcome of work was the minimum permissible distance of overhead and trackside installations from high-speed rail, which was obtained through simulation with finite element software. The permissible distance obtained for a railway with maximum train speed of 350 km/h are as depicted in Table 5.

Table 5. Permissible distance of overhead and trackside installations from the high-speed train

Distance (m)	Permissible distance
From the ground	$d \in (4.85, 6.25)$
From the train's centerline	$L \in (3.32, 4.25)$

In this table, a lower limit and a higher limit are presented for the permissible distance of the location of obstacles. That is, if an obstacle is closer to the train than the lower limit of the permissible distance, this will lead to damage to the structure given that the stress exerted on the structure will exceed its yield stress. If an obstacle is farther from the train than the upper limit of the permissible distance, the obstacle

will sustain no damage given that the stress exerted will be almost negligible. Therefore, the aforesaid obstacle (a pipe with a diameter of 2 inches) can be situated within the distance between the calculated lower limit and upper limit and suffer no damage.

List of symbols

d_h	Hydraulic diameter (m)
h	Train height (m)
p	Aerodynamic pressure (Pa)
$\bar{p}$	Time-averaged aerodynamic pressure (Pa)
V_w	Wind speed amplitude (m/s)
C_p	Aerodynamic pressure coefficient
k	Turbulence kinetic energy (m^2/s^{-2})
y^+	Dimensionless distance to the wall
d	Barrier distance from ground (m)
L	Barrier distance from the train's centerline (m)
(u,v,w)	Wind speed components in direction (x,y,z)
$(\bar{u},\bar{v},\bar{w})$	Time-averaged wind speed component in direction (x,y,z)
$(\bar{u}',\bar{v}',\bar{w}')$	Fluctuating components of wind speed in direction (x,y,z)

Greek symbols

ρ	Air density
ε	Dissipation rate

References

[1] D.R. Tiwari, N. Sharma, P. Khatri, S. Panwar, Design and analysis of Maglev trains, Global Journal for Research Analysis, Vol.5, (2016).

[2] C. TSI, 648, Commission decision concerning a technical specification for interoperability relating to the rolling stock sub-system of the trans-European high-speed rail system, Technical report, official journal of the European union, (2008).

[3] T. Hara, M. Kawaguti, G. Fukuchi, A. Yamamoto, Aerodynamics of high-speed train, in Monthly Bulletin of the International Railway Congress Association, (1968), pp.121-146.

[4] H. Hemida, N. Gil, C. Baker, LES of the slipstream of a rotating train, Journal of Fluids Engineering, Vol. 132, (2010).

[5] H. Hemida, C. Baker, G. Gao, The calculation of train slipstreams using large-eddy simulation, Proceedings of the Institution of Mechanical Engineers, Part F: Journal of Rail and Rapid Transit, Vol. 228, (2014), pp.25-36.

[6] T. W. Muld, Slipstream and flow structures in the near wake of high-speed trains, KTH Royal Institute of Technology, (2012).

[7] C. Baker, S. Jordan, T. Gilbert, A. Quinn, M. Sterling, T. Johnson, J. Lane, Transient aerodynamic pressures and forces on trackside and overhead structures due to passing trains. Part 1: Model-scale experiments; Part 2: Standards applications, Proceedings of the Institution of Mechanical Engineers, Part F: Journal of Rail and Rapid Transit, Vol. 228, (2014), pp.37-70.

[8] Y. Dhanabalan, Numerical study of a wind tunnel setup for measuring train slipstream with Detached Eddy Simulation, (2013).

[9] N. Yang, X.-K. Zheng, J. Zhang, S. Law, Q.-s. Yang, Experimental and numerical studies on aerodynamic loads on an overhead bridge due to passage of high-speed train, Journal of Wind Engineering and Industrial Aerodynamics, Vol. 140, (2015), pp.19-33.

[10] N. Axelsson, M. Ramnefors, R. Gustafsson, Accuracy in computational aerodynamics Part 1: Stagnation pressure, SAE Technical Paper, (1998).

[11] X. Zhang, P. Wu, W. Shang, W. Chen, S. Gao, Research on the parallel partition performance of high-speed train with aerodynamic brake based on Fluent, in Computer and Information Technology (CIT), 2012 IEEE 12th International Conference on, (2012), pp.1029-1033.

[12] L.Q. Gao, Y. Xi, Q. Fu, M.H. Zhu, J.S. Zhang, Performance analysis of a new type of wind resistance brake mechanism based on FLUENT and ANSYS,in advanced materials Research, (2012), pp.1099-1102.

[13] Z. Jianyong, W. Mengling, T. Chun, X. Ying, L. Zhuojun, C. Zhongkai, Aerodynamic braking device for high-speed trains: Design, simulation and experiment, Proceedings of the Institution of Mechanical Engineers, Part F:

Journal of Rail and Rapid Transit, Vol.228, (2014), pp.260-270.

[14] M. Puharić, S. Linić, D. Matić, V. Lučanin, Determination of braking force of aerodynamic brakes for high speed trains, Transactions of FAMENA, Vol. 35, (2011).

[15] M. Manhart, H. Wengle, A spatiotemporal decomposition of a fully inhomogeneous turbulent flow field, Theoretical and computational fluid dynamics, Vol.5, (1993), pp.223-242.

[16] S. Krajnovic, Numerical simulation of the flow around an ICE2 train under the influence of a wind gust, in Railway Engineering-Challenges for Railway Transportation in Information Age, 2008. ICRE 2008. International Conference on, (2008), pp. 1-7.

[17] M. Ghazanfari, P. Hosseini Tehrani, Study on braking panels in high speed trains using CFD, Advances in Railway Engineering, An International Journal, Vol. 2, (2014), pp.93-106.

[18] T. Stathopoulos, The numerical wind tunnel for industrial aerodynamics: Real or virtual in the new millennium, Wind and Structures, Vol. 5, (2002), pp.193-208.

[19] T. Ogawa, K. Fujii, Numerical investigation of three-dimensional compressible flows induced by a train moving into a tunnel, Computers & Fluids, Vol. 26, (1997), pp.565-585.

[20] M. Howe, Mach number dependence of the compression wave generated by a high-speed train entering a tunnel, Journal of Sound and Vibration, Vol. 212, (1998), pp.23-36,.

[21] A. M. Biadgo, A. Simonović, J. Svorcan, S. Stupar, Aerodynamic characteristics of high speed train under turbulent cross winds: A numerical investigation using unsteady-RANS method, FME Transactions, Vol. 42, (2014), pp.10-18.

[22] M. Casey, T. Wintergerste, S. Innotec, ERCOFTAC special interest group on quality and trust in industrial CFD, Best practice guidelines, (2000).

[23] F. Guillou, CFD Study of the Flow around a High-Speed Train, (2012).

[24] T. Gilbert, C. Baker, A. Quinn, M. Sterling, Aerodynamics of high-speed trains in confined spaces, in Proceedings of the 7th International Colloquium on Bluff Body Aerodynamics and Applications, (2012).

[25] M.-l. Wu, Y.-y. Zhu, C. Tian, W.-w. Fei, Influence of aerodynamic braking on the pressure wave of a crossing high-speed train, Journal of Zhejiang University-SCIENCE A, Vol. 12, (2011), pp.979-984.

[26] B. STANDARD, Seamless and welded steel tubes—Dimensions and masses per unit length, (2002).